


Article

Reductive Dechlorination of Chloroacetamides with NaBH_4 Catalyzed by Zero Valent Iron, ZVI, Nanoparticles in ORMOSIL Matrices Prepared via the Sol-Gel Route

Michael Meistelman ¹ , Dan Meyerstein ^{2,3,*}, Amos Bardea ⁴, Ariela Burg ⁵, Dror Shamir ⁶ and Yael Albo ^{1,*}

¹ Chemical Engineering Dept. and The Centre for Radical Reactions, Ariel University, Ariel 4070000, Israel; michaelme@ariel.ac.il

² Department of Chemical Sciences and The Centre for Radical Reactions, Ariel University, Ariel 4070000, Israel

³ Chemistry Dept., Ben-Gurion University, Beer-Sheva 8410501, Israel

⁴ Faculty of Engineering, Holon Institute of Technology (HIT), Holon 5810201, Israel; amos.bardea@hit.ac.il

⁵ Department of Chemical Engineering, Shamoon College of Engineering, Beer-Sheva 8410802, Israel; arielab@ac.sce.ac.il

⁶ Department of Chemistry, Nuclear Research Centre Negev, Beer-Sheva 8419001, Israel; drorshamir@gmail.com

* Correspondence: danm@ariel.ac.il (D.M.); yaelyt@ariel.ac.il (Y.A.)

Received: 5 July 2020; Accepted: 20 August 2020; Published: 1 September 2020



Abstract: The efficient reductive dechlorination, as remediation of dichloroacetamide and monochloroacetamide, toxic and abundant pollutants, using sodium borohydride catalyzed by zero valent iron nanoparticles (ZVI-NPs), entrapped in organically modified hybrid silica matrices prepared via the sol-gel route, ZVI@ORMOSIL, is demonstrated. The results indicate that the extent of the dechlorination reaction depends on the nature of the substrate and on the reaction medium. By varying the amount of catalyst or reductant in the reaction it was possible to obtain conditions for full dechlorination of these pollutants to nontoxic acetamide and acetic acid. A plausible mechanism of the catalytic process is discussed. The present work expands the scope of ZVI-NP catalyzed reduction of polluting compounds, first reports the catalytic parameters of chloroacetamide reduction, and offers additional insight into the heterogeneous catalyst structure of M^0 @ORMOSIL sol-gel. The ZVI@ORMOSIL catalyst is ferromagnetic and hence can be recycled easily.

Keywords: catalysis; zero valent iron; de-chlorination; borohydride; sol-gel; ferromagnetic

1. Introduction

Halogenated hydrocarbons are known to be toxic pollutants [1]. More than half a century ago it was proposed to study each halogenated compound independently of its homologue hydrocarbon series [1]. While there are number of halogenated pollutants that are monitored by the health authorities, e.g., halo-acetic acids, others which appear on the EPA's (United States Environmental Protection Agency) contaminant candidate list await proper directives and legislation, e.g., halo-acetamides which are formed during chlorination of drinking water [2]. Halo-organic compounds can be reduced electro-chemically [3,4], photo-chemically [5], radiolytically [6], and by a variety of reducing agents [7]. These processes often require a catalyst [8]. M^0 -nano-particles (M^0 -NPs), e.g., Ag^0 -NPs and Au^0 -NPs [9,10], are often used as catalysts for these processes [11–14], thus enabling the reduction of these compounds to their non-toxic or less toxic and environmentally friendly products.

Zero valent iron (ZVI) is a feasible solution to environmental applications due to its reactivity, high abundance, and relatively low cost [15,16]. ZVI has been widely studied as a reducing agent for the remediation treatment of halogenated hydrocarbon pollutants in the environment, both for contaminated soils and for water sources [17,18]. Other applications involve the adsorption of toxic heavy metal cation such as lead and arsenic [19–21] and of organic pollutants such as tetracycline [22], which might reduce the risk of increasing antibiotics resistance. It is also used in Fenton-based oxidations, for example, to remove amoxicillin [23] and to remove TNT from water sources [20].

However, ZVI forms surface oxides/hydroxides in an aerobic environment that dramatically reduce the reaction rates, and therefore, ZVI is not used in batch processes that must be completed on a short timescale [24]. The activity of ZVI can be improved by adding Cu^0 to the system [25,26], probably due to a galvanic effect. It was shown that a weak magnetic field enhances the dehalogenation of tri-haloacetamides, however, mono-chloro-acetamides are not reduced [27]. ZVI can also be used as catalyst. For example, when paired with NaBH_4 as a reducing agent, it was shown to optimize the reduction of nitrophenol [28–30].

Recently it was shown that ZVI-NPs entrapped in sol-gel matrices can be used as effective heterogeneous catalysts for reductive dehalogenation reactions (RDH) of halo-acetic acids [31]. The high yields and the stability of the catalyst suggest its plausible use for the reduction of the more toxic and very abundant chloroacetamides family of pollutants [2,32–34]. To the best of our knowledge, there has been no attempt to date to utilize ZVI-NPs as a catalyst in the reductive dehalogenation of chloroacetamides. The strategy of degrading dichloroacetamide (DCAm) in various reaction media has not been reported yet. Shedding light on DCAm reduction reactivity and the mechanism of reductive dehalogenation reaction in different solvents can help elucidate better ways of disposing of this hazardous pollutant and offer a versatile strategy towards remediation of various environmental pollutants of the same group. In the current study, it is shown that ZVI-NPs entrapped in organically modified silica (ORMOSIL) matrices (ZVI@ORMOSIL), prepared via the sol-gel route, are useful catalysts for the reductive dehalogenation of dichloroacetamide with NaBH_4 , yielding acetamide and acetate as the final harmless products.

2. Results and Discussion

2.1. 1.0 M ZVI-NPs Ethanolic Suspension

The 1.0 M ZVI-NPs suspension, prepared from the 25 nm ZVI commercial powder, was analyzed using transmission electron microscopy to ensure that no major agglomeration had occurred in the suspension used for preparation of the catalyst (Figure 1). Although agglomerated macro-particles are observed, they largely consist of recognizable nanosized ZVI spheres that fall in the nanometer range, <100 nm. Hence, they are suitable to be used as nano-catalysts. This colloidal suspension was used in the ZVI@ORMOSIL catalyst preparation.

The ethanolic suspension shows magnetic properties that were observed by simple magnet-induced moving of the suspended ZVI powder within the solution.

Photon cross correlation spectroscopy measurements were performed to estimate the initial particle aggregation degree due to interaction of the particles in the suspension. The results obtained support the TEM findings indicating some agglomeration of the ZVI NPs (Figure 2). Although it might be suspected that the agglomerated particles that are observed in Figure 1 might originate from solvent evaporation that occurred while placing the suspension sample on the grid, the average values of Sauter mean diameter (SMD), 95.5 nm, and volume mean diameter (VMD) of 95.5 nm, measured for 25 nm ZVI commercial powder in 1.0 M ethanolic suspension, show that agglomeration of a similar degree occurs in the suspension.



Figure 1. TEM micrograph of 1.0 M ethanolic suspension of commercial 25 nm zero valent iron nanoparticles (ZVI-NPs).

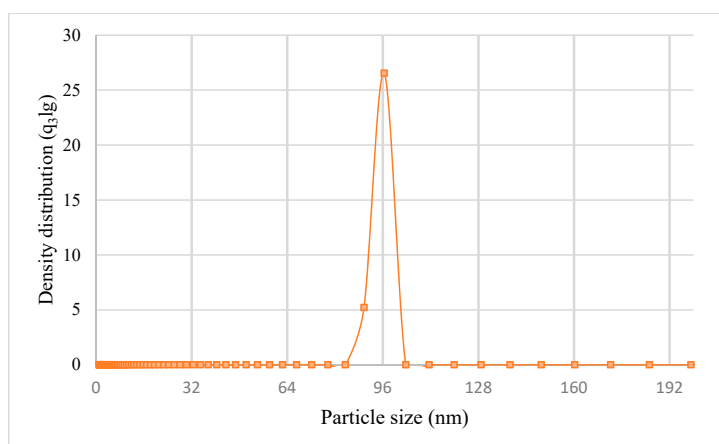


Figure 2. Particle size distribution of 1.0 M ethanolic suspension of commercial 25 nm ZVI-NPs.

ZVI@ORMOSIL Synthesis via the Sol-Gel Route

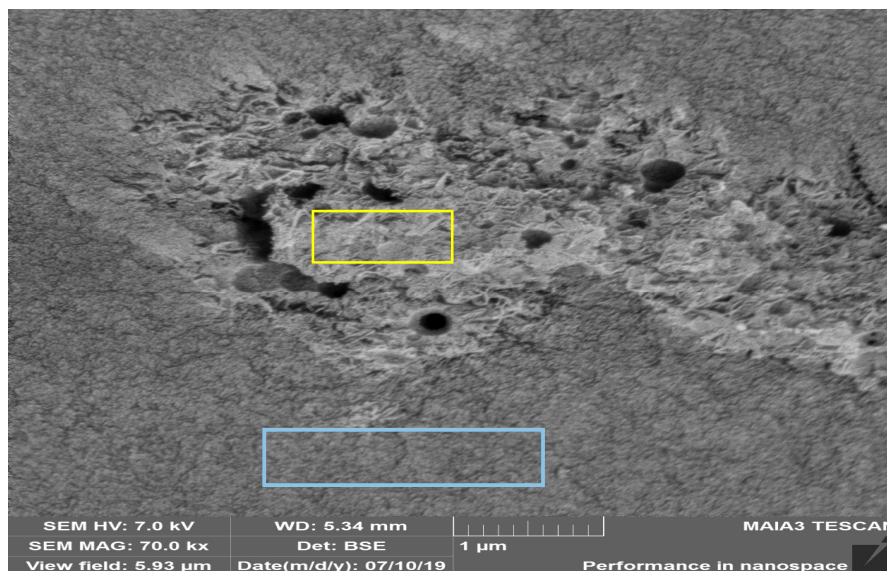
The differences between ZVI@ORMOSIL gel forms in different preparation steps are visualized in Figure S1. As the wet gel dries in the desiccator, the raw gel undergoes shrinkage due to cooperative action between hydrolysis and densification [35]. In the final stages of the preparation, the dried gel is crushed into powder using a mortar and pestle. The obtained powder has magnetic properties (Figure 3).



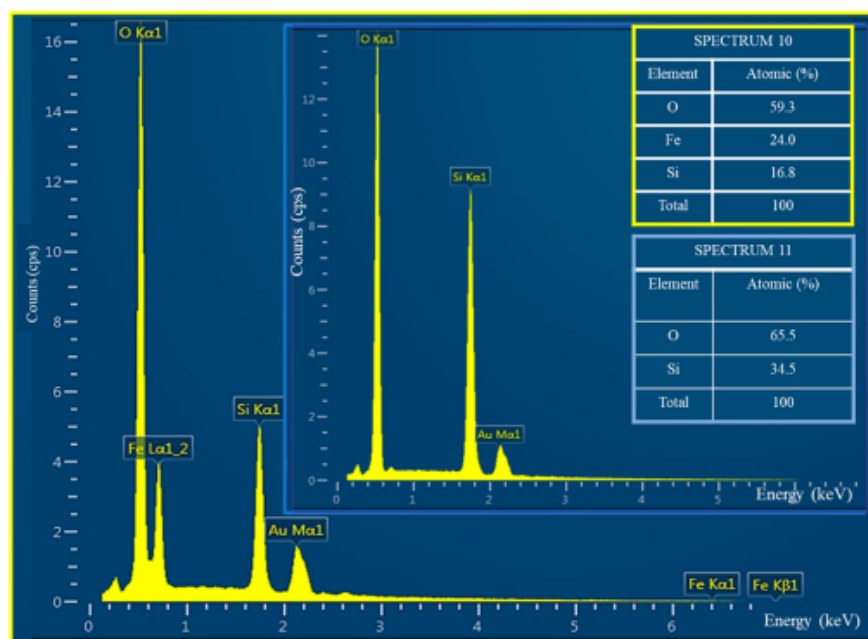
Figure 3. Dry grinded ZVI@ORMOSIL powder on a magnetic bar.

2.2. Catalyst Characterization

To investigate the surface morphology and to determine the elemental composition of 1.0% ZVI@ORMOSIL, STEM/EDAX analysis was performed (Figure 4).



(a)



(b)

Figure 4. Scanning electron microscopy image and elemental composition of ZVI@ORMOSIL catalyst matrix. (a) SEM image of 1.0% ZVI@ORMOSIL matrix. (b) Elemental composition measured by electron dispersive analysis in two areas marked in (a); Spectrum 10, measured near cracks and breaks in the matrix-yellow frame; Spectrum 11, measured in the monolith bulk of ZVI@ORMOSIL matrix-blue frame.

The results indicate that the amorphous ORMOSIL surface comprises many cracks, probably due to non-uniform shrinkage and densification of the matrix in the drying stage of the sol-gel process. The elemental composition spectra were taken from two regions of the monolith, marked in Figure 4a.

Near the cracks and breaks formed in the structure, the composition shows the presence of elemental iron (spectrum 10). Conversely, signals collected from the uniform part of the bulk (spectrum 11) exhibit no significant elemental iron. Nevertheless, traces of elemental iron might be present on the monolith surface. It is possible that ZVI will not be detected if it is at a low concentration level and below the sensitivity level of the specific apparatus. A surface composition sensitive method, XPS, was applied to ensure more precise iron detection, as shown below.

Discrimination between successful entrapment in the voids of the bulk material and surface immobilization is possible by measuring the surface composition. To characterize the surface composition of the ZVI@ORMOSIL catalyst, XPS analysis was used. The survey scan of the whole range of 1.0% load ZVI@ORMOSIL is presented in Figure 5. Silicon and oxygen were successfully observed. The carbon detected is probably that of the methyl groups in the matrix originating from the methyltrimethoxysilane precursor. Focused scans for iron content led to detection of almost negligible traces, close to the baseline noise level, as shown in the insert of Figure 5. Using manual sample manipulation, a successful integration extracted a sample area that was calculated as 0.2% atomic of the whole sample area that was scanned in the analysis. Although iron was found as a part of the surface composition, as summarized in Table S1, the almost negligible amounts confirm that most of the catalyst was entrapped within the bulk of the hybrid silica host structure. These findings indicate that the ZVI is trapped in the pores, and they exclude the unwanted possibility of significant surface immobilization of the catalyst.

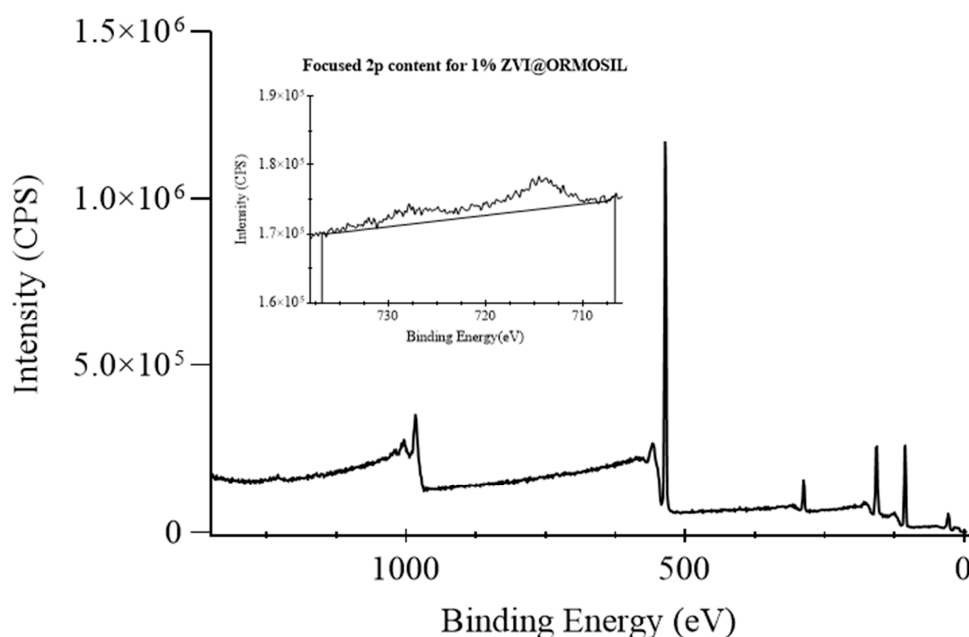


Figure 5. XPS spectra of 1.0% load ZVI@ORMOSIL. Insert: focused scan on Fe^0 peak.

Three types of samples were analyzed using powder X-ray diffraction, PXRD: the original 1.0 M suspension of ZVI used in the preparation of matrices, 1.0% ZVI-NP load ZVI@ORMOSIL, and 10% load ORMOSIL, which was prepared to aid the identification of ZVI phases. Incorporation of low amounts of ZVI nanoparticles in the bulk structure might result in diffraction patterns that are obscured due to the amorphous silica baseline signal. Figure 6 shows a comprehensive overlap among phases found in the original ZVI suspension that was used in the preparation of 1.0% and 10% load ZVI@ORMOSIL, as summarized in Table 1. Major phases were seen at 44.7° and 65.1° , fitting the 1,1,0 and 2,0,0 plains of Fe^0 phases. The slight presence of a Fe_3O_4 phase was also confirmed with peaks at 35.4° and 62.5° . These findings fall in line with the expected observations since an almost neglectable catalyst presence was found in the surface layers of the gel and considerable presence was confirmed for the penetrative XRD analysis of ZVI@ORMOSIL.

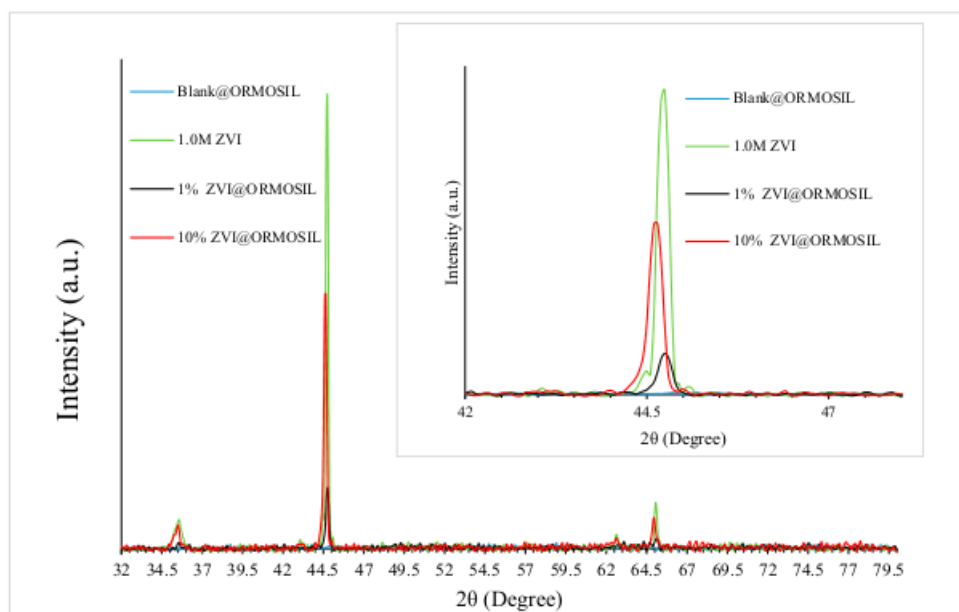


Figure 6. PXRD diffractograms. Blank@ORMOSIL—black, 1.0 M ZVI ethanolic suspension—blue, 10% mol load ZVI@ORMOSIL—green, 1.0% mol load ZVI@ORMOSIL—red.

Table 1. Metal phases found in ZVI@ORMOSIL.

Substance	2θ	Miller Index	File No.
Fe ⁰	44.7°	1,1,0	04-007-9753
Fe ⁰	65.1°	2,0,0	
Fe ₃ O ₄	35.4°	3,1,1	04-005-4319
Fe ₃ O ₄	62.5°	4,0,0	

The Scherrer equation was used to calculate the average crystallite size (D_p , nm). Reflection parameters at 44.7° and 65.1° were used for the calculation; the results were averaged and are summarized in Table 2 (all the relevant phases and card numbers files are given in the Supplementary Materials (SI-3)). A certain agglomeration extent might be attributed to the influence of ammonium hydroxide [36] introduced in the preparation of ZVI@ORMOSIL (2% NH₃, 1.5 mL). Similarly prepared catalysts previously reported [31] had an average crystallite size of 34.5 nm, as calculated from the powder XRD results. It was noted that a ZVI secondary particle might comprise many primary crystallites.

Table 2. Average crystallite size.

Material	D_p (nm)
1.0 M susp.	44.9
10% ZVI@ORMOSIL	38.8
1% ZVI@ORMOSIL	34.7

A descriptive ORMOSIL sol-gel pore system and framework study of the catalyst structure was performed using N₂ adsorption-desorption studies. Surface area and pore volumes for 1.0% ZVI@ORMOSIL and for the blank@ORMOSIL matrix without nanoparticles are summarized in Table 3. Both the host matrix without particles and the entrapped catalyst matrix have large surface areas and narrow distributions of the inner pores that are in the mesoporous range. The pore size distributions (diameter) are presented in Figure S4. Surprisingly, the doped matrix has a larger pore volume and surface area; this result suggests that the agglomeration of the gel is affected by the presence of

ZVI-NPs added during the gelation stage. The larger surface area of ZVI@ORMOSIL induces the reaction substrates to be adsorbed more onto its surface.

Table 3. N₂ adsorption-desorption isotherms summary.

Sample	Surface Area (m ² /g)	Average Pore Volume (cm ³ /g)	Average Pore Diameter (nm)
Blank@ORNOSIL	574	0.53	4.7
1.0% ZVI@ORMOSIL	751	0.73	4.7

The N₂ adsorption-desorption isotherms presented in Figure 7 can be classified as type IV isotherms with H2A hysteresis loops. The asymmetrical shape of these H2A hysteresis loop types (as per current IUPAC convention [37]) are typical for porous glass [38]. These loops describe a distribution of pore sizes and shapes with bottleneck constrictions [39]. They are characteristic of interconnected ink-bottle pores rather than isolated, individual ink-bottle pores, as an “assembly of cavities connected by constrictions” [39]. These findings correspond to previously reported organically modified silica (ORMOSIL) matrices prepared by mixing a large variety of precursors [40,41]. Similar hysteresis loops were previously reported for ORMOSIL entrapped metal nanoparticles used in the reductive dehalogenation of halo-acetic acids [13].

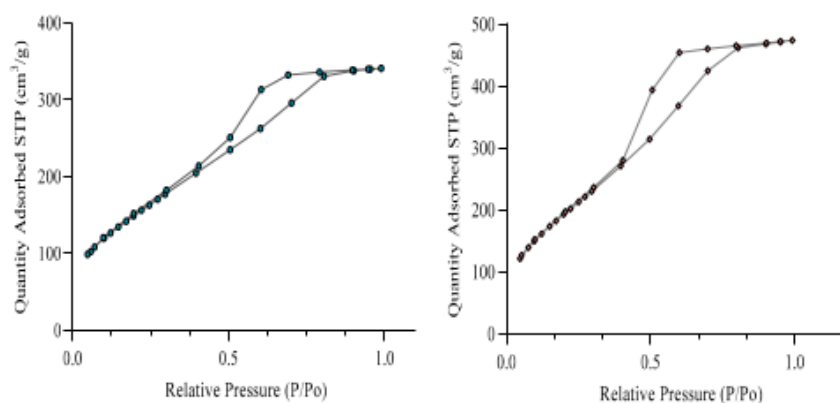


Figure 7. N₂ adsorption-desorption isotherms Blank@ORMOSIL (left) and 1.0% ZVI@ORMOSIL (right).

2.3. Catalytic Reductive Dehalogenation

2.3.1. Dehalogenation of Di- and Mono-Chloroacetamides

The reductions of monochloroacetamide (MAcAm), dichloroacetamide (DAcAm), and of solutions containing both substrates at a 1:1 molar ratio were performed in different reaction media. The reactions were performed at an initial pH of 8.0 with a constant substrate:NaBH₄ molar ratio of 1:20, if not otherwise stated. The products distributions obtained under each reaction condition are summarized in Table 4.

To check the reduction rates of ZVI alone as a reducing agent, typical dehalogenation reactions of both DAcAm and MAcAm were performed, the absence of the sodium borohydride addition step being the only difference. These reactions were continued for 24 h with no reduction yields worth mentioning. Thus, the NaBH₄ addition is required. NaBH₄ was added to the homogenized suspension of the substrates and catalysts and 2.0 mL of water was added shortly afterward to ensure the full dissolution of NaBH₄. The products analysis was performed 15 min later. This time frame choice was designed to assist in the mechanistic study displaying the distribution of the reaction products under various conditions. The plausible reduction products for DAcAm; MAcAm, acetamide (AcAm),

Acetic acid (AA), and ammonia are given in reaction (1) and the product distributions obtained by its reduction are presented in Figure 8.

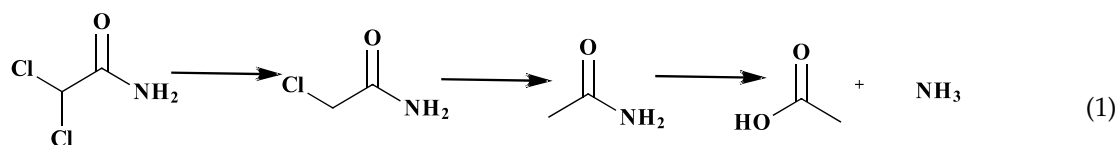


Table 4. The medium effect on dehalogenation yields of DAcAm and MAcAm *.

Starting Subs.	Medium	DAcAm (%)	MAcAm (%)	AcAm (%)	AA (%)
DAcAm	H ₂ O	0	76	18	6
MAcAm		0	53	47	0
DAcAm/MAcAm, (1/1)		0	65	31	3
DAcAm	EtOH:H ₂ O 8:2	22	63	10	5
MAcAm		0	84	16	0
DAcAm/MAcAm, (1/1)		12	75	13	3
DAcAm	ACN:H ₂ O 8:2	46	52	2	0
MAcAm		0	80	20	0
DAcAm/MAcAm, (1/1)		23	66	11	0
DAcAm	2-PrOH:H ₂ O 8:2	60	40	0	0
MAcAm		0	90	10	0
DAcAm/MAcAm, (1/1)		30	65	5	0

* 8.8 mM and 4.4 mM DAcAm and MAcAm were reduced with [NaBH₄] = 0.176 M, 0.10 g ZVI@ORMOSIL, for 15 min at room temperature, initial pH 8.0.

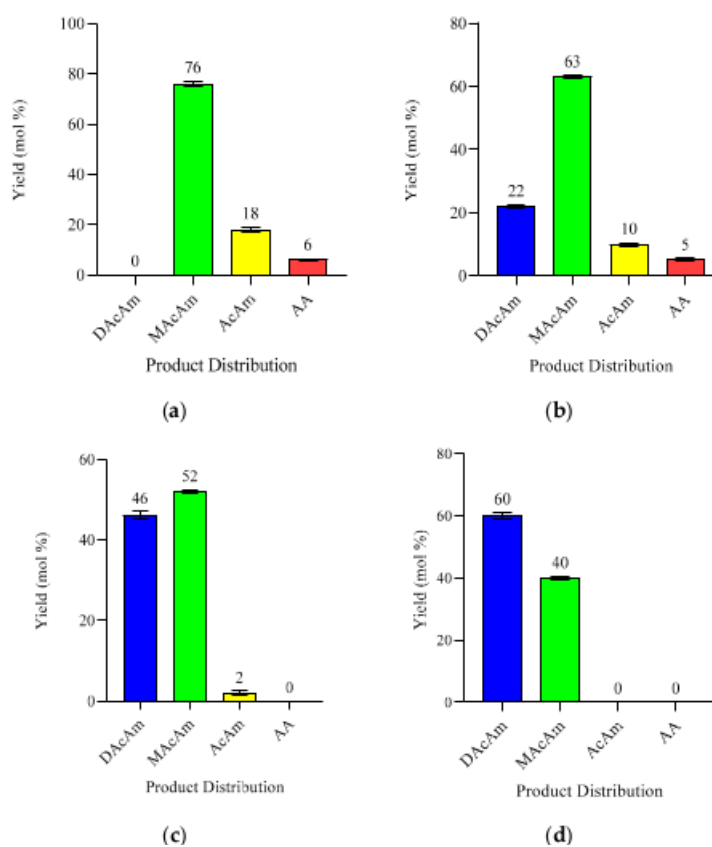
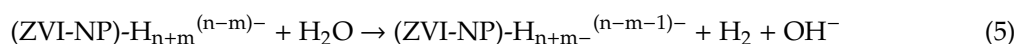
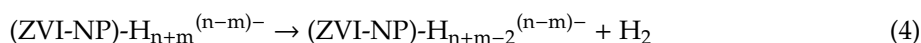
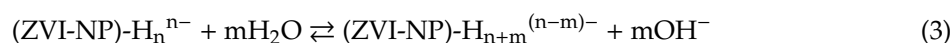


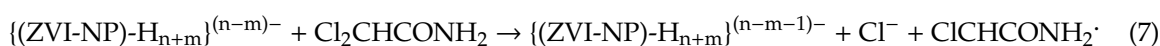
Figure 8. Products distributions of dehalogenation of dichloroacetamide performed in different reaction media. [DAcAm] = 8.8 mM, [NaBH₄] = 0.176 M, 0.10 g catalyst, reaction medium: (a) deaerated water; (b) 8:2 (EtOH:H₂O); (c) 8:2 (CH₃CN:H₂O); (d) 8:2 (2-Propanol:H₂O).

The results in Table 4 suggest that:

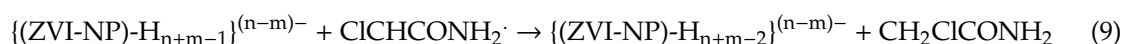
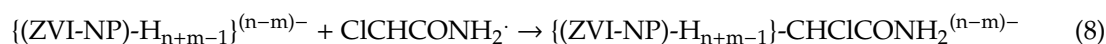
I. The BH_4^- will first reduce the surface hydroxides/oxides of the ZVI-NPs. Then, it is expected to form $(\text{ZVI-NP})\text{-H}_{n+m}^{(n-m)-}$ via reactions (2) and (3) [31]. In the absence of an oxidizing agent, these reactions are followed by reactions (4) and/or (5) [31]. In the presence of an oxidizing substrate, reactions (4) and (5) always compete with the reduction process.



II. The dehalogenation of the chloro-acetamides by BH_4^- is expected to follow an analogous mechanism to the dechlorination of $\text{Cl}_3\text{CCO}_2^-$ [31]. As $\text{B}(\text{OH})_3$ formed in reaction (2) is a buffer with a $\text{pK}_b = 4.9$ and as OH^- is formed in reactions (3) and (5), the reaction media are always slightly alkaline. The first step in the de-halogenation process is expected to follow either reaction (6), which is a hydrogen transfer process, or reaction (7), which is an electron transfer process; in both, the radical $\text{ClCHCONH}_2\cdot$ is formed.



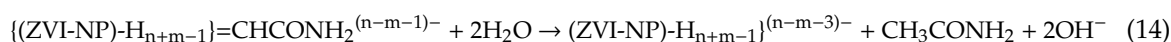
This radical is expected to react with the $\{(\text{ZVI-NP})\text{-H}_{n+m-1}\}^{(n-m)-}/\{(\text{ZVI-NP})\text{-H}_{n+m}\}^{(n-m-1)-}$ nanoparticles via reactions (8) and/or (9). It should be noted that analogous reactions to reaction (8) [42,43] and (9) [44] were reported to be fast.



The $\{(\text{ZVI-NP})\text{-H}_{n+m-1}\}\text{-CHClCONH}_2^{(n-m)-}$ formed in reaction (8) might decompose via reactions (10)–(13):

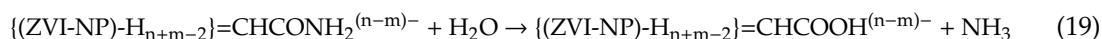
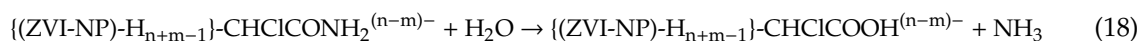


The $\{(\text{ZVI-NP})\text{-H}_{n+m-1}\}=\text{CHCONH}_2^{(n-m-1)-}/\{(\text{ZVI-NP})\text{-H}_{n+m-2}\}=\text{CHCONH}_2^{(n-m)-}$ formed in the latter reactions will decompose via reactions (14)–(17).



III. The observation that in the aqueous and ethanolic media, acetic acid is formed only from the DAcAm and not from the MAcAm proves that partially the

$\{(ZVI-NP)-H_{n+m-1}\}-CHClCONH_2^{(n-m)-}$ does not decompose via reactions (9)–(11) and that the decomposition of the $\{(ZVI-NP)-H_{n+m-1}\}-CHClCONH_2^{(n-m)-}$ and/or the $\{(ZVI-NP)-H_{n+m-1}\} = CHCONH_2^{(n-m-1)-} / \{(ZVI-NP)-H_{n+m-2}\} = CHCONH_2^{(n-m)-}$ intermediates, or at least one of them, involves the hydrolysis of the amide group prior to the loss of the second chloride or prior to the decomposition of the $ZVI=CH-$ bond (reactions (17) or (18)). The latter bond type is not formed during the dechlorination of MAcAm.



The MAcAm product formed in the dechlorination of DAcAm occurs via one or more of reactions (9)–(11).

IV. The results indicate that the nature of the solvent, though enough water is always present, affects the mechanism of the dehalogenation considerably. At present, the data available do not enable us to determine at what stage of the process this is crucial.

The relative difficulty in performing MAcAm dechlorination in comparison with the dechlorination of DAcAm is attributed to the relative stabilities of the C-Cl bonds.

It was subsequently decided to check whether increasing the amount of the catalyst or the $[BH_4^-]$ will enable full dechlorination.

2.3.2. Catalyst Dosing Dehalogenation Experiments

The results presented in Figure 9 indicate that the increase of the catalyst amount suspended in the reaction solution considerably improves the dechlorination process.

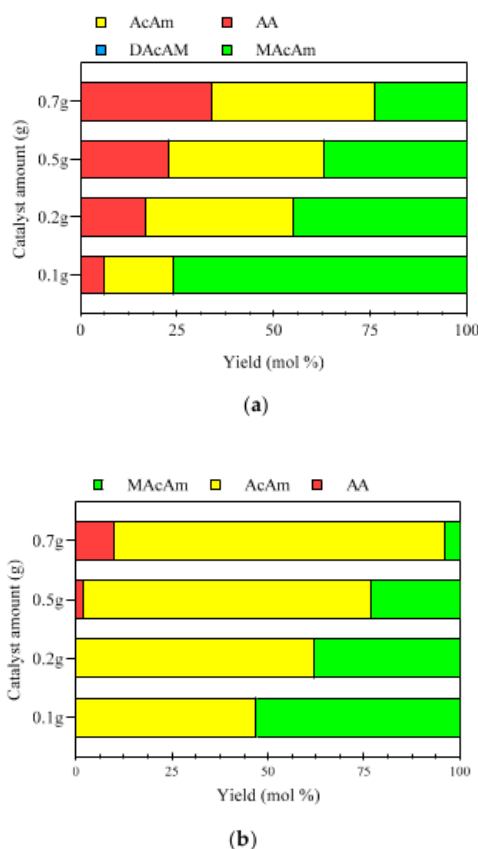


Figure 9. ZVI@ORMOSIL catalyzed reduction of DAcAm (a) and MAcAm (b) at increasing catalyst weight. [substrate] = 8.8 mM, $[NaBH_4]$ = 0.176 M, reaction medium: water.

The catalyst amount introduced in the reaction has considerable impact on the degree of dechlorination. The ability to reduce the yield of MAcAm to 24% in the reduction of DAcAm, Figure 9a, and the dechlorination by 86% of MAcAm, Figure 9b, is significant. A plausible explanation is that with the decrease in the ratio $[\text{BH}_4^-]/[\text{catalyst}]$, the charge on the ZVI-NPs decreases, which slows down reactions (4) and (5), which compete with the dechlorination process.

Surprisingly, at the high catalyst concentration, some acetic acid is formed during the dechlorination of MAcAm. This contradicts the discussion above. A plausible explanation is that the intermediates formed during the dechlorination of MAcAm are $\{(ZVI\text{-}NP)\text{-}H_{n+m-k}\}\text{-}(\text{CH}_2\text{CONH}_2)_k^{(n-m)-}$ and not $\{(ZVI\text{-}NP)\text{-}H_{n+m-1}\}\text{-}CH_2\text{CONH}_2^{(n-m)-}$. The number of $\text{-CH}_2\text{CO-NH}_2$ bound to a given ZVI-NP affects its properties and a smaller number slows down the ZVI-C bond heterolysis facilitating the amide hydrolysis.

2.3.3. NaBH_4 Dosing Dechlorination Experiments

The dependence of the distribution of the products on $[\text{BH}_4^-]$ is presented in Figure 10. The results of these experiments indicate that, as expected, an increase in the $[\text{BH}_4^-]/[\text{substrate}]$ ratio increases the dechlorination yield, though the ratio $[\text{dechlorinated products}]/[\text{BH}_4^-]$ decreases.

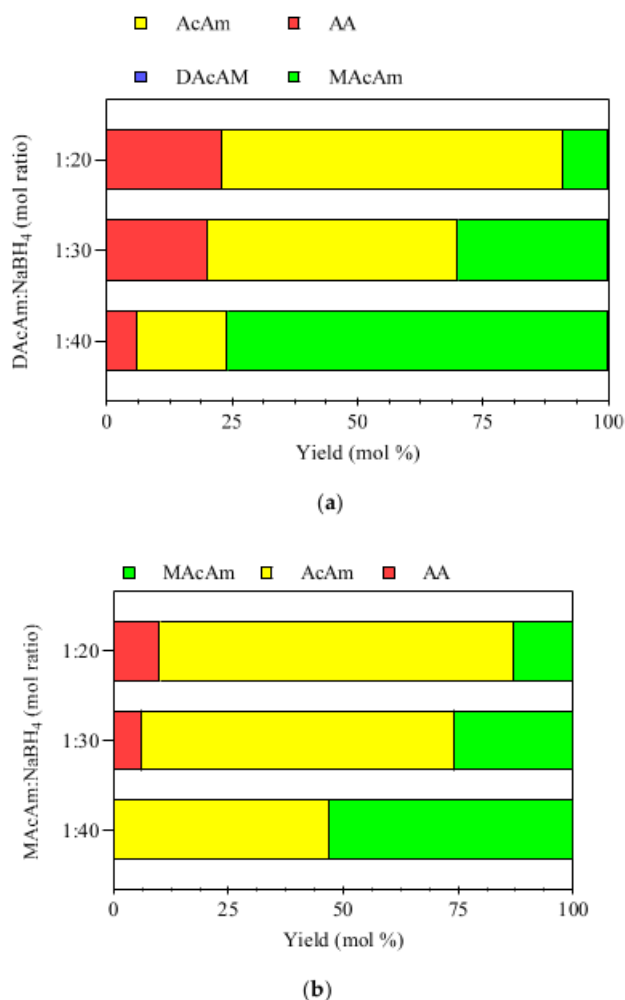


Figure 10. Effect of $[\text{NaBH}_4]$ on the product distribution. The reaction suspensions in water contained 0.10 g catalyst at room temperature. Reaction time 15 min. (a) $[\text{DAcAm}] = 8.8 \text{ mM}$; (b) $[\text{MAcAm}] = 8.8 \text{ mM}$.

However, here too at high $[\text{BH}_4^-]$, the dechlorination of MAcAm yields some acetic acid. This is probably due to the increase in the number of H-atoms/hydrides, $n+m$, bound to the same ZVI-NP coherently. The effect of these hydrogens on the properties of the NPs is similar to that of the $-\text{CH}_2\text{CONH}_2$ groups discussed in the previous section.

In an effort to fully dechlorinate DACAm and MAcAm, a combination of use of high catalyst amounts, 0.70 g of ZVI@ORMOSIL, and high $[\text{BH}_4^-]/[\text{substrate}] = 40:1$ was performed. For DACAm as substrate, the yields were only 7% of MacAm, 57% of AcAm, and 36% of AA. For MAcAm, the yields were 10% of MAcAm, 78% of AcAm, and 12% of AA, i.e., full dechlorination was not achieved. In a last set of experiments, full dechlorination of MAcAm was achieved by performing an identical experiment but delivering the same amount of NaBH_4 in two doses. The first dose was allowed to react for 15 min and then the second portion was added for another 15 min. In this experiment, the final products consisted of 63% of acetamide and 37% acetic acid, i.e., 100% dechlorination.

2.3.4. Catalyst Stability Test

To check the recyclability of ZVI@ORMOSIL in the dechlorination of DACAm, 8 consecutive reactions were performed. For each dehalogenation reaction cycle, the same catalyst was utilized. Before each cycle, the matrix was washed with distilled water and dried. No significant effect on the products distribution was observed (Figure 11).

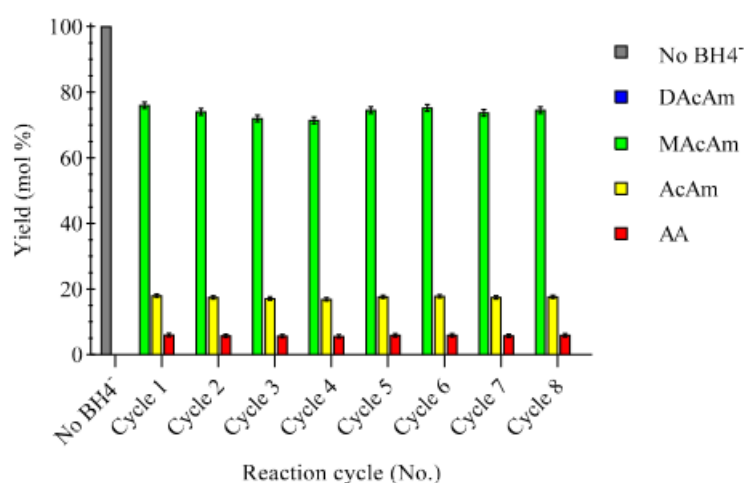


Figure 11. Dechlorination of DACAm in repeated use of the catalyst. The dechlorination was performed in water following 15 min cycles, $[\text{DACAm}] = 8.8 \text{ mM}$, $[\text{NaBH}_4] = 0.176 \text{ M}$, 0.10 g catalyst.

3. Materials and Methods

3.1. Materials

Tetraethylorthosilane (TEOS) > 99%, methyltrimethoxysilane (MTMOS) (97%), zerovalent iron nanoparticles (ZVI-NPs) as iron 25 nm nanopowder > 98.0%, hydrochloric acid (HCl, 37%) and 85% H_3PO_4 were purchased from Sigma-Aldrich ®(Rehovot, Israel). Sodium borohydride (98%), dichloroacetamide (DACAm) (>96%), monochloroacetamide (MAcAm) (>96%), acetamide (AcAm) (>97%), acetic acid (AA) (99%) were purchased from Alfa Aesar (Heysham, England). LCMS grade solvents, ethanol (EtOH), acetonitrile (ACN), and 2-propanol, were purchased from Bio-Lab Ltd. (Jerusalem, Israel). All chemicals were used as received. All aqueous solutions were prepared from deionized water purified using a Millipore Milli-Q set up (Merck, Darmstadt, Germany) with a final resistivity of >10 $\text{M}\Omega/\text{cm}$.

3.2. Synthesis

3.2.1. Preparation of ZVI-NP Suspension

An amount of 0.56 g of 25 nm iron nanoparticles powder was suspended in 10.0 mL of ethanol (AR) resulting in 1.0 M ZVI suspension sealed and stored under nitrogen at 4 °C, equilibrated to room temperature before use.

3.2.2. ZVI@ORMOSIL Synthesis via the Sol-Gel Route

1.0% mol load ZVI@ORMOSIL

The catalyst was prepared by using the two steps acid/base sol-gel synthesis route. Briefly, 37% HCl (62 μ L, 2.53 μ mol) was dissolved in water (2.72 g, 0.151 mol), and the mixture was added slowly into a premixed solution containing MTMOS (1.556 g, 0.011 mol) and TEOS (5.6 g, 0.027 mol), which were dissolved in ethanol (7.02 g, 0.152 mol). The resulting mixture was homogenized for 15 min. A 2.0% NH₃ solution (1.5 mL, 7.7 mmol) was then added to the mixture dropwise. When the gelation started, 380 μ L of 1.0 M ethanolic suspension of ZVI was added and the mixture was stirred vigorously. The wet black gel was kept for 15 days for aging and drying at room temperature. The solid matrix obtained was crushed with a mortar and pestle into a powder and washed with water several times. The washed matrix was then dried and used for the catalytic tests. A tenfold volume of 1.0 M ZVI suspension was used to obtain 10% mol load ZVI@ORMOSIL catalyst.

3.3. Catalyst Characterization

Transmission microscopy images, electron microscopy, and elemental composition were obtained using a 3FE-Tescan ultra high resolution MAIA microscope with an AZTEC microanalysis EDX detector, Oxford Instruments, Colorado, USA. Suspension mean particle size was measured using photon cross correlation spectroscopy (PCCS) with nanophox/R (Sympatec, Germany). The data was analyzed using WINDOX 5. Sample suspensions were sonicated for 10 min in an ultrasonic water bath at room temperature. The measurement was done in a 4 mL plastic cuvette placed in a temperature-controlled water bath. The readings were performed at 632.8 nm. Ethanol (LCMS) RI 1.362, viscosity 1.071 mPas (25 °C).

X-ray diffraction (XRD) measurements were performed with a Bruker (Karlsruhe, Germany) AXS D8 ADVANCE Series II diffractometer equipped with a LynxEye detector (reflection θ – θ geometry, Cu K α radiation (λ = 0.154 nm), divergence slit 0.60 mm, anti-scattering slit 8.0 mm). Diffraction data were collected in the angular range of $10^\circ < 2\theta < 80^\circ$, step size 0.05° , and a step time of 0.5 sec/step. N₂ adsorption-desorption isotherms were measured using an APP gold instruments VSorb 2800 model surface area and porosity analyzer, sensitivity 0.010 m²/g, range 2–500 nm pore size. Specific surface area, average pore size distribution (PSD), pore volume, and adsorption-desorption isotherms were measured in analyses performed using Brunauer–Emmett–Teller (BET) and Barrett–Joyner–Halenda (BJH) methods on a BET surface analyzer. XPS surface analysis was performed using a Thermo Fisher Scientific (East Grinstead, United Kingdom) NEXSA XPS system with monochromatized Al K α source (400 micron diameter). Pass Energy (“resolution”) of 200 eV was used for survey scans to obtain a general surface composition profile and 50 eV for the high-resolution scans that were used for quantitative analysis.

3.4. Catalytic Tests

Dichloroacetamide and monochloroacetamide were taken as model substrates to study the catalytic activity of ZVI@ORMOSIL towards reductive dehalogenation. In a typical catalytic dehalogenation experiment, ZVI@ORMOSIL was weighed (ca. 0.10 g) in a glass vial, 16.90 mg of dichloroacetamide or 12.34 mg of monochloroacetamide (8.8 mM of each substrate) was accurately transferred to the vial. 13 mL of a solvent (deaerated water, ethanol, acetonitrile or 2-propanol) was added, then 0.10 g of NaBH₄ was accurately added to the vessel, composing a relative excess ratio of 1:20 (0.132 mmol

of substrate/2.64 mmol NaBH₄). Finally, 2.0 mL of deuterated water was added to complete a total reaction volume to 15 mL. In a comparative dehalogenation experiment, half of the amount of each substrate was transferred to the same vial in the same preparation method to obtain 1:1 mole/mole mixture, 8.5 mg of DAcAm, and 6.2 mg of MAcAm, yielding 4.4 mM of each substrate in the final reaction solution. The resulting suspensions were stirred for 15 min, and after that, the catalyst was recovered using filtration, and the filtrate was analyzed using HPLC. The reaction samples, standards, and blanks were diluted and filtered before RP-HPLC monitoring for the degradation of haloacetamides. Ammonia amounts are equimolar to the monitored acetic acid for obvious reasons.

HPLC analysis was performed on a Dionex Ultimate 3000 equipped with a Diode Array Detector by Thermo Hypersil-gold C18 1504.6 mm 3 μm column. Acetic acid, dichloroacetamide, monochloroacetamide, and acetamide were eluted by (0.10% H₃PO₄; ACN), (4:96) mobile phase, 0.6 mL/min flow, 23 °C column temp, with UV detection at 200 nm, 5.0 μL injection volume. The reaction samples were quenched with a few drops of diluted H₃PO₄, filtered through 0.22 μm PES or H-PTFE according to the reaction solvent, and all samples were diluted and adjusted to pH 3.0 if necessary, filtered with 0.22 μm PES filter membrane before analysis.

Spectroscopic analysis of ammonia was performed according to a reported procedure [45–48]. Briefly, 0.10 mL of 1.62 M ethanolic solution of phenol was added to 2.5 mL of the filtered reaction solution. After vigorous stirring, 0.10 mL of 0.50% *w/v* of hexacyanoferrate trihydrate in water was added. After additional stirring, 0.25 mL of the oxidizing solution comprising alkaline 0.64 M citrate trihydrate and 0.12% NaOCl was added, and the standard solutions were prepared likewise. The samples were covered with aluminum foil and kept in the dark at ambient temperature to let the color develop. Absorbances were recorded at 640 nm in 1.0 cm quartz cuvettes. A Varian Cary UV Bio 50 spectrophotometer with dual-beam, Czerny-Turner monochromator, Xenon pulse lamp single source, and dual Si diode detector was used (Agilent technologies, Middleburg, The Netherlands).

4. Conclusions

To conclude, a facile room temperature synthesis of 1% load ZVI@ORMOSIL catalyst via the sol-gel route was performed. The interconnected bottleneck constrictions may contribute to diffusion-controlled rates of dehalogenations. ZVI@ORMOSIL heterogeneous robust catalyst exhibits a good extent of dehalogenation of haloacetamides, producing fully dehalogenated reaction products. Thus, zero valent iron ORMOSIL immobilized nanoparticles prove to be a worthy replacement in reactions catalyzed with rare and expensive metals. The stability of M⁰-C formed as an intermediate is a crucial step for determining which solvent mixture may be best for performing the shown reactions.

This report broadens the scope of use of ZVI immobilized in sol-gel as a heterogeneous catalyst for environmental remediation applications. A previously reported use of ZVI as a reductant obtained a noteworthy dehalogenation of haloacetamides, but not to the full dehalogenation extent [25–27]. A complete dehalogenation of DAcAm and MAcAm is reported herein, obtaining fully detoxified acetamide and acetic acid products.

Supplementary Materials: The following are available online at <http://www.mdpi.com/2073-4344/10/9/986/s1>, Figure S1: (a) Raw wet ORMOSIL gel, (b) crushed ZVI@ORMOSIL gel; Figure S2: Powder diffraction file for Fe0 phases; Figure S3: Powder diffraction file for Fe3O4 phases; Figure S4: (a) pore size distribution for Blank@Ormosil, (b) pore size distribution for 1% ZVI@Ormosil; Table S1: XPS surface analysis elemental composition of 1% ZVI@ORMOSIL.

Author Contributions: Conceptualization, D.M., Y.A., A.B. (Amos Bardea), D.S. and A.B. (Amos Burg); methodology, Y.A., M.M. and D.M.; Funding acquisition, D.M., Y.A. and A.B. (Amos Bardea); Investigation, M.M., Y.A., A.B. (Amos Bardea) and D.M. All authors have read and agreed to the published version of the manuscript.

Funding: This study was enabled in part by a grant from the HIT & Ariel University Joint Research Fund.

Acknowledgments: M. Meistelman thanks the Ariel University for a Ph.D. Fellowship.

Conflicts of Interest: The authors declare no conflict of interest.

References

1. Dragstedt, C.A. The halogenated hydrocarbons: Their toxicity and potential dangers. *AMA Arch. Intern. Med.* **1956**, *97*, 261–262. [[CrossRef](#)]
2. Kimura, S.Y.; Vu, T.N.; Komaki, Y.; Plewa, M.J.; Mariñas, B.J. Acetonitrile, and N-Chloroacetamide formation from the reaction of Acetaldehyde and Monochloramine. *Environ. Sci. Technol.* **2015**, *49*, 9954–9963. [[CrossRef](#)] [[PubMed](#)]
3. Martin, E.T.; McGuire, C.M.; Mubarak, M.S.; Peters, D.G. Electroreductive remediation of halogenated environmental pollutants. *Chem. Rev.* **2016**, *116*, 15198–15234. [[CrossRef](#)]
4. Borojovich, E.J.C.; Bar-Ziv, R.; Oster-Golberg, O.; Sebbag, H.; Zinigrad, M.; Meyerstein, D.; Zidki, T. Halo-organic pollutants: The effect of an electrical bias on their decomposition mechanism on porous iron electrodes. *Appl. Catal. B* **2017**, *210*, 255–262. [[CrossRef](#)]
5. Letourneau, D.R.; Gill, C.G.; Krogh, E.T. Photosensitized degradation kinetics of trace halogenated contaminants in natural waters using membrane introduction mass spectrometry as an in-situ reaction monitor. *Photochem. Photobiol. Sci.* **2015**, *14*, 2108–2118. [[CrossRef](#)]
6. Trojanowicz, M.; Drzewicz, P.; Pańta, P.; Głuszewski, W.; Nałecz-Jawecki, G.; Sawicki, J.; Sampa, M.H.O.; Oikawa, H.; Borrelly, S.I.; Czaplicka, M.; et al. Radiolytic degradation and toxicity changes in g-irradiated solutions of 2,4-dichlorophenol. *Radiat. Phys. Chem.* **2002**, *65*, 357–366. [[CrossRef](#)]
7. Kar, P.; Mishra, B.G. Hydrodehalogenation of halogenated organic contaminants from aqueous sources by Pd nanoparticles dispersed in the micropores of pillared clays under transfer hydrogenation condition. *J. Clust. Sci.* **2014**, *25*, 1463–1478. [[CrossRef](#)]
8. Heveling, J. Heterogeneous Catalytic chemistry by example of industrial applications. *J. Chem. Educ.* **2012**, *89*, 1530–1536. [[CrossRef](#)]
9. Zidki, T.; Bar-Ziv, R.; Green, U.; Cohen, H.; Meisel, D.; Meyerstein, D. The effect of the nano-silica support on the catalytic reduction of water by gold, silver and platinum nanoparticles–nanocomposite reactivity. *Phys. Chem. Chem. Phys.* **2014**, *16*, 15422–15429. [[CrossRef](#)] [[PubMed](#)]
10. Zidki, T.; Cohen, H.; Meyerstein, D.; Meisel, D. Effect of silica-supported silver nanoparticles on the dihydrogen yields from irradiated aqueous solutions. *J. Phys. Chem. C* **2007**, *111*, 10461–10466. [[CrossRef](#)]
11. Adhikary, J.; Meistelman, M.; Burg, A.; Shamir, D.; Meyerstein, D.; Albo, Y. Reductive dehalogenation of monobromo- and tribromoacetic acid by sodium borohydride catalyzed by gold nanoparticles entrapped in sol-gel matrices follows different pathways. *Eur. J. Inorg. Chem.* **2017**, *11*, 1510–1515. [[CrossRef](#)]
12. Meistelman, M.; Adhikary, J.; Burg, A.; Shamir, D.; Gershinsky, G.; Meyerstein, D.; Albo, Y. Ag⁰ and Au⁰ nanoparticles encapsulated in sol-gel matrices as catalysts in reductive de-halogenation reactions. *Chim. Oggi.* **2017**, *35*, 23–26.
13. Adhikary, J.; Meyerstein, D.; Marks, V.; Meistelman, M.; Gershinsky, G.; Burg, A.; Shamir, D.; Kornweitz, H.; Albo, Y. Sol-gel entrapped Au⁰- and Ag⁰-nanoparticles catalyze reductive de-halogenation of halo-organic compounds by BH₄⁻. *Appl. Catal. B-Environ.* **2018**, *239*, 450–462. [[CrossRef](#)]
14. Trabelsi, K.; Meistelman, M.; Ciriminna, R.; Albo, Y.; Pagliaro, M. Effective and green removal of trichloroacetic acid from disinfected water. *Materials* **2020**, *13*, 827–828. [[CrossRef](#)]
15. Ludwig, J.R.; Schindler, C.S. Catalyst: Sustainable catalysis. *Chemicals* **2017**, *2*, 313–316. [[CrossRef](#)]
16. Kaushik, M.; Moores, A. New trends in sustainable nanocatalysis: Emerging use of earth abundant metals. *Curr. Opin. Green Sust.* **2017**, *7*, 39–45. [[CrossRef](#)]
17. MacCrehan, W.A.; Bedner, M.; Helz, G.R. Making chlorine greener: Performance of alternative dechlorination agents in wastewater. *Chemosphere* **2005**, *60*, 381–388. [[CrossRef](#)]
18. Ibrahim, A.K.; Moghny, T.A.; Mustafa, Y.M.; Maysour, N.E.; El-Din El-Dars, F.M.S.; Hassan, R.F. Degradation of trichloroethylene contaminated soil by zero-valent iron nanoparticles. *ISRN Soil Sci.* **2012**, 1–10. [[CrossRef](#)]
19. Bagbi, Y.; Sarswat, A.; Tiwari, S.; Mohan, D.; Pandey, A.; Solanki, P.R. Nanoscale zero-valent iron for aqueous lead removal. *Adv. Mat. Proc.* **2017**, *2*, 235–241. [[CrossRef](#)]
20. Fu, F.; Dionysiou, D.D.; Liu, H. The use of zero-valent iron for groundwater remediation and wastewater treatment: A review. *J. Hazard. Mater.* **2014**, *267*, 194–205. [[CrossRef](#)]
21. Kharisov, B.I.; Rasika Dias, H.V.; Kharissova, O.V.; Jiménez-Pérez, V.M.; Pérez, B.O.; Flores, B.M. Iron-containing nanomaterials: Synthesis, properties, and environmental applications. *RSC Adv.* **2012**, *2*, 9325–9358. [[CrossRef](#)]

22. Guler, U.A. Removal of tetracycline from aqueous solutions using nanoscale zero valent iron and functional pumice modified nanoscale zero valent iron. *J. Environ. Eng. Landsc.* **2017**, *25*, 223–233. [[CrossRef](#)]
23. Zha, S.; Cheng, Y.; Gao, Y.; Chen, Z.; Megharaj, M.; Naidu, R. Nanoscale zero-valent iron as a catalyst for heterogeneous Fenton oxidation of amoxicillin. *Chem. Eng. J.* **2014**, *255*, 141–148. [[CrossRef](#)]
24. Shea, P.J.; Machacek, T.A.; Comfort, S.D. Accelerated remediation of pesticide-contaminated soil with zerovalent iron. *Environ. Pollut.* **2004**, *132*, 183–188. [[CrossRef](#)] [[PubMed](#)]
25. Chu, W.; Li, X.; Bond, T.; Gao, N.; Bin, X.; Wang, Q.; Ding, S. Copper increases reductive dehalogenation of haloacetamides by zero-valent iron in drinking water: Reduction efficiency and integrated toxicity risk. *Water Res.* **2016**, *107*, 141–150. [[CrossRef](#)] [[PubMed](#)]
26. Chen, S.; Chu, W.; Wei, H.; Zhao, H.; Xu, B.; Gao, N.; Yin, D. Reductive dechlorination of haloacetamides in drinking water by Cu/Fe bimetal. *Sep. Purif. Technol.* **2018**, *203*, 226–232. [[CrossRef](#)]
27. Chen, S.; Wang, F.; Chu, W.; Li, X.; Wei, H.; Gao, N. Weak magnetic field accelerates chloroacetamide removal by zero-valent iron in drinking water. *Chem. Eng. J.* **2019**, *358*, 40–47. [[CrossRef](#)]
28. Bouazizi, N.; Vieillard, J.; Bargougui, R.; Couvrat, N.; Thoumire, O.; Morin, S.; Ladam, G.; Mofaddel, N.; Brun, N.; Azzouz, A.; et al. Entrapment and stability of iron nanoparticles within APTES modified graphene oxide sheets with improved catalytic activity. *J. Alloy. Compd.* **2019**, *771*, 1090–1102. [[CrossRef](#)]
29. Sravanthi, K.; Ayodhya, D.; Swamy, P.Y. Green synthesis, characterization, and catalytic activity of 4-nitrophenol reduction and formation of benzimidazoles using bentonite supported zero valent iron nanoparticles. *Mater. Sci. Energy Technol.* **2019**, *2*, 298–307. [[CrossRef](#)]
30. Bae, S.; Gim, S.; Kim, H.; Hanna, K. Effect of NaBH₄ on properties of nanoscale zero-valent iron and its catalytic activity for reduction of p-nitrophenol. *Appl. Catal. B-Environ.* **2016**, *182*, 541–549. [[CrossRef](#)]
31. Meyerstein, D.; Adhikary, J.; Burg, A.; Shamir, D.; Albo, A. Zero-valent iron nanoparticles entrapped in SiO₂ sol-gel matrices: A catalyst for the reduction of several pollutants. *Catal. Commun.* **2020**, *133*, 1–5. [[CrossRef](#)]
32. Plewa, M.J.; Muellner, M.G.; Richardson, S.D.; Fasano, F.; Buettner, K.M.; Woo, Y.; McKague, A.B.; Wagner, E.D. Occurrence, synthesis, and mammalian cell cytotoxicity and genotoxicity of haloacetamides: An emerging class of nitrogenous drinking water disinfection byproducts. *Environ. Sci. Technol.* **2008**, *42*, 955–961. [[CrossRef](#)] [[PubMed](#)]
33. Chu, W.; Gao, N.; Yin, D.; Krasner, S.W. Formation, and speciation of nine haloacetamides, an emerging class of nitrogenous DBPs, during chlorination or chloramination. *J. Hazard. Mater.* **2013**, *260*, 806–812. [[CrossRef](#)] [[PubMed](#)]
34. Chu, W.; Li, D.; Gao, N.; Templeton, M.R.; Tan, C.; Gao, Y. The control of emerging haloacetamide DBP precursors with UV/persulfate treatment. *Water Res.* **2015**, *72*, 340–348. [[CrossRef](#)] [[PubMed](#)]
35. Brinker, C.J.; Scherer, G.W. *Sol-Gel Science: The Physics and Chemistry of Sol-Gel Processing*; Academic Press: Boston, MA, USA, 1990.
36. Andrade, A.L.; Fabris, J.D.; Ardisson, J.D.; Valente, M.A.; Ferreira, J.M.F. Effect of Tetramethylammonium Hydroxide on nucleation, surface modification and growth of magnetic nanoparticles. *J. Nanomater.* **2012**, *15*, 1–10. [[CrossRef](#)]
37. Thommes, M.; Kaneko, K.; Neimark, A.V.; Olivier, J.P.; Rodriguez-Reinoso, F.; Rouquerol, J.; Sing, K.S.W. Physisorption of gases, with special reference to the evaluation of surface area and pore size distribution. *Pure Appl. Chem.* **2015**, *87*, 1–19. [[CrossRef](#)]
38. Grosman, A.; Ortega, C. Capillary condensation in porous materials hysteresis and interaction mechanism without pore blocking/percolation process. *Langmuir* **2008**, *24*, 3977–3986. [[CrossRef](#)]
39. Alothman, Z.A. A review: Fundamental aspects of silicate mesoporous materials. *Materials* **2012**, *5*, 2874–2902. [[CrossRef](#)]
40. Santos, A.M.; Vasconcelos, W.L. Obtention of nanostructured silica glass by sol-gel process with incorporation of lead compounds. *Mater. Res.* **1999**, *2*, 201–204. [[CrossRef](#)]
41. Lenza, R.F.S.; Vasconcelos, W.L. Preparation of silica by sol-gel method using formamide. *Mater. Res.* **2001**, *4*, 189–194. [[CrossRef](#)]
42. Rusonik, I.; Cohen, H.; Meyerstein, D. Cu (I) (2,5,8,11-tetramethyl-2,5,8,11-tetraazadodecane) as a catalyst for Ullmann's reaction. *J. Chem. Soc. Dalton Trans.* **2003**, *10*, 2024–2028. [[CrossRef](#)]
43. Zidki, T.; Cohen, H.; Meyerstein, D. Reactions of alkyl-radicals with gold and silver nanoparticles in aqueous solutions. *Phys. Chem. Chem. Phys.* **2006**, *8*, 3552–3556. [[CrossRef](#)] [[PubMed](#)]

44. Bar-Ziv, R.; Zidki, T.; Zilbermann, I.; Yardeni, G.; Meyerstein, D. Effect of hydrogen pretreatment of platinum nanoparticles on their catalytic properties: Reactions with alkyl radicals—a mechanistic study. *Chem. Cat. Chem.* **2016**, *8*, 2761–2764. [[CrossRef](#)]
45. Solorzano, L. Determination of ammonia in natural waters by the phenol hypochlorite. *Method. Limnol. Oceanogr.* **1969**, *14*, 799–801. [[CrossRef](#)]
46. Park, G.; Oh, H.; Ahn, S. Improvement of the ammonia analysis by the phenate method in water and wastewater. *B Korean Chem. Soc.* **2009**, *30*, 2032–2038. [[CrossRef](#)]
47. Rhine, E.D.; Sims, G.K.; Mulvaney, R.L.; Pratt, E.J. Improving the Berthelot reaction for determining ammonium in soil extracts and water. *Soil Sci. Soc. Am. J.* **1998**, *62*, 473–480. [[CrossRef](#)]
48. Kimble, K.W.; Walker, J.P.; Finegold, D.N.; Asher, S.A. Progress toward the development of a point-of-care photonic crystal ammonia sensor. *Anal. Bioanal. Chem.* **2006**, *385*, 678–685. [[CrossRef](#)]



© 2020 by the authors. Licensee MDPI, Basel, Switzerland. This article is an open access article distributed under the terms and conditions of the Creative Commons Attribution (CC BY) license (<http://creativecommons.org/licenses/by/4.0/>).